Research Article **Open Access**

Jan Jarvis*, Marko Haertelt, Stefan Hugger, Lorenz Butschek, Frank Fuchs, Ralf Ostendorf, Joachim Wagner and Juergen Beyerer

Hyperspectral data acquisition and analysis in imaging and real-time active MIR backscattering spectroscopy

DOI 10.1515/aot-2016-0068
Received December 9, 2016; accepted February 6, 2017; previously published online March 30, 2017

Abstract: In this work we present data analysis algorithms for detection of hazardous substances in hyperspectral observations acquired using active mid-infrared (MIR) backscattering spectroscopy. We present a novel background extraction algorithm based on the adaptive target generation process proposed by Ren and Chang called the adaptive background generation process (ABGP) that generates a robust and physically meaningful set of background spectra for operation of the well-known adaptive matched subspace detection (AMSD) algorithm. It is shown that the resulting AMSD-ABGP detection algorithm competes well with other widely used detection algorithms. The method is demonstrated in measurement data obtained by two fundamentally different active MIR hyperspectral data acquisition devices. A hyperspectral image sensor applicable in static scenes takes a wavelength sequential approach to hyperspectral data acquisition, whereas a rapid wavelength-scanning single-element detector variant of the same principle uses spatial scanning to generate the hyperspectral observation. It is shown that the measurement timescale of the latter is sufficient for the application of the data analysis algorithms even in dynamic scenarios.

Keywords: active stand-off spectroscopy; hyperspectral data analysis; QCL.

***Corresponding author: Jan Jarvis,** Fraunhofer Institute for Applied Solid State Physics, (IAF), Tullastrasse 72, 79108 Freiburg, Germany, e-mail: jan-philip.jarvis@iaf.fraunhofer.de
Marko Haertelt, Stefan Hugger, Lorenz Butschek, Frank Fuchs, Ralf Ostendorf and Joachim Wagner: Fraunhofer Institute for Applied Solid State Physics (IAF), Freiburg, Germany
Juergen Beyerer: Fraunhofer Institute of Optronics, System Technologies and Image Exploitation (IOSB), Karlsruhe Institute of Technologie (KIT), Karlsruhe, Germany

www.degruyter.com/aot

1 Introduction

Stand-off detection of hazardous substance residues has been subject to extensive research in the past few years, and yet remains to pose an ambitious goal. For successful application under real-world conditions high true positive and low false alarm rates are required. Besides measurement speed, mobility and system robustness additional requirements may also include unperceived and eye-safe operation in uncontrolled environments (e.g. avoiding operation of high power lasers). Though numerous approaches have been published, to this day none were able to solve the task, matching all of the given conditions.

Among the suggested methods, laser-based measurement techniques have emerged as the most promising. Van Neste et al. proposed a trace explosive detection system based on photoacoustic spectroscopy using quantum cascade lasers (QCLs) [1]. Kendziora et al. reported impressive results using an approach called *photothermal infrared imaging spectroscopy* that also employs QCLs for spectrally selective illumination [2]. Östmark et al. developed a stand-off imaging Raman spectroscopy device for trace explosive detection [3], whereas Gottfried et al. employed laser-induced breakdown spectroscopy for the same task [4].

1.1 Data analysis

Robust data analysis algorithms form a crucial component of hyperspectral detection systems, and several solutions have been proposed in the past few decades, many of which are based on the linear mixture model (LMM). The LMM assumes that the observed spectra can be described as linear superposition of contributing pure material spectra that form the columns of the matrix $\mathbf{S} = [\mathbf{s}_1 \cdots \mathbf{s}_q]$ and which are commonly referred to as *endmembers*. Mathematically, the LMM reads

$$\mathbf{x}_i = \mathbf{S}\cdot\boldsymbol{\alpha}_i + \mathbf{n}_i,\ \mathbf{S}\in\mathbb{R}^{p\times q},\ \boldsymbol{\alpha}_i\in\mathbb{R}^q,\ \mathbf{n}_i\in\mathbb{R}^p. \quad (1)$$

The abundances $\boldsymbol{\alpha}_i = [\alpha_{i1}\cdots\alpha_{iq}]^\top$ comprise the relative mixture weights for a specific observation $\mathbf{x}_i$. Zero mean Gaussian normal distributed noise with band-independent variance σ is usually assumed for the noise vector $\mathbf{n}\sim\mathrm{N}(\mathbf{0}, \sigma^2\mathbf{I})$. Target detection algorithms that employ the LMM are in general capable of sub-pixel detection as the background spectral contribution is part of the model design. In contrast, full pixel target detection algorithms such as the constraint energy minimization (CEM) [5], the matched filter (MF), e.g. given in [6], as well as the normalized cross correlation (NCC) were proposed that do not require a specific data model. Well-known *sub-pixel target detection algorithms* that employ the LMM are the orthogonal subspace projection (OSP), the adaptive matched subspace detector (AMSD) and the adaptive coherence/cosine estimator (ACE) [7]. The AMSD and ACE algorithms take a hypotheses testing approach to target detection by estimating a likelihood ratio for the two competing hypotheses, that a pixel vector contains the target substance, or consists of background material only. Whereas the ACE detector models the background as random noise distribution, the AMSD explicitly models the background using the contributing background endmembers. These are unknown in a generic measurement scenario and thus have to be estimated from the available data. Based on Ren and Chang's adaptive target generation process (ATGP) [8], we present an algorithm called the adaptive background extraction process (ABGP) in Section 2 that solves this task in a two-step process.

1.2 Evaluation data

The algorithm is tested on measured data using two different experimental approaches. Both hyperspectral sensors are based on active mid-infrared (MIR) spectroscopy using external cavity QCLs (EC-QCLs) as illumination sources and have been subject to previous publications. The hyperspectral imaging sensor described in [9] acquires a full hyperspectral image at the timescale of 10 s and is shown to be well applicable for residue detection in static scenes. However, as the hyperspectral image bands are sequentially generated, a relative motion of the sensor and scene could potentially induce non-linear spectral mixing of adjacent materials in the resulting data set. In [10] a fast scanning single-element detector variant of the same principle is proposed that measures single spectra at a timescale of 1 ms and the required spatial information is obtained sequentially. It is shown that the measurement speed is sufficient for acquisition of hyperspectral observations in dynamic scenes (i.e. scenes that contain objects moving at a limited speed or spatial displacement caused by data acquisition using a hand-held device) without violation of the assumptions made by the mixture model. Consequently, the proposed target detection algorithms are readily applicable to measurement data obtained by either system.

2 The adaptive background generation process

The ABGP is an iterative endmember extraction algorithm that generates the background endmember matrix in two stages. In the seeding stage, it searches for image spectra that are most different from each other and the target spectrum using Ren and Chang's ATGP [8], which employs ideas lent from the OSP target detection algorithm to generate a set of q potential pure substance estimates. In the subsequent *stabilization stage*, a clustering method is employed to obtain more significant class representatives.

2.1 The seeding stage

In the seeding stage given in Listing 1 a set of potential background spectra that form the columns of the seed matrix $\tilde{\mathbf{B}}$ is generated. This is achieved by operating the ATGP algorithm and initializing the endmember matrix with the target matrix $\mathbf{T}\in\mathbb{R}^{p\times t}$. In this variant the ATGP is expected to identify potential pure background pixels, while avoiding target spectra. We thus refer to the columns of $\mathbf{T}$ as *include guards*.

Listing 1: The ABGP seeding stage as a variant of the ATGP algorithm.

Input: Hyperspectral observation $\mathbf{X}=\{\mathbf{x}_i\}_{i=1}^N$, $\mathbf{x}\in\mathbb{R}^p$, target matrix $\mathbf{T}\in\mathbb{R}^{p\times t}$, background dimension q
Output: Background seed vectors $\tilde{\mathbf{B}}=[\tilde{\mathbf{b}}_1, \ldots, \tilde{\mathbf{b}}_q]$
\\ initialize background matrix with include guards
$\tilde{\mathbf{B}}\leftarrow\mathbf{T}$
for $j\leftarrow 1$ **to** q **do**
\\ find spectrum that differs most from target and background
$\mathbf{P}_{\tilde{\mathbf{B}}}^{\perp}\leftarrow\mathbf{I}-\tilde{\mathbf{B}}(\tilde{\mathbf{B}}^\top\tilde{\mathbf{B}})^{-1}\tilde{\mathbf{B}}$
$\tilde{\mathbf{b}}\leftarrow\mathrm{argmax}_{\mathbf{x}_i}\{(\mathbf{P}_{\tilde{\mathbf{B}}}^{\perp}\mathbf{x}_i)^\top(\mathbf{P}_{\tilde{\mathbf{B}}}^{\perp}\mathbf{x}_i)\}$
$\tilde{\mathbf{B}}\leftarrow$ concatenate $\tilde{\mathbf{B}}, \tilde{\mathbf{b}}$
\\drop include guards
$\tilde{\mathbf{B}}\leftarrow[\tilde{\mathbf{b}}_{t+1}, \ldots, \tilde{\mathbf{b}}_{t+q}]$
return $\tilde{\mathbf{B}}$

The result of the seeding stage is a set of background seeding vectors $\tilde{\mathbf{B}} = [\tilde{\mathbf{b}}_1, \ldots, \tilde{\mathbf{b}}_q]$ that could already be used as background endmembers for a target detection algorithm. However, in that case only a small fraction of the available data are employed for model construction. In addition, single pixel spectra can be subject to noise artifacts and the ATGP which is based on an extreme value measure intrinsically favors outliers. This can substantially affect the quality of $\tilde{\mathbf{B}}$. We propose a stabilization stage that runs a clustering algorithm on the observation data using $\tilde{\mathbf{B}}$ as seed vectors and adopt the cluster means as background endmembers.

2.2 The stabilization stage

A seed-based strict partitioning of the observation data $\{\mathbf{x}_i\}_{i=1}^N$ into $q+t$ clusters $\{C_1, \ldots, C_q, C_{q+1}, \ldots, C_{q+t}\}$ is obtained using any full-pixel target detection algorithm. Let $T(\mathbf{x}_i; \mathbf{v})$ denote the corresponding target detection function for the observation vector $\mathbf{x}_i$ and target vector $\mathbf{v}$. As the value of T relates to the probability that $\mathbf{x}_i$ contains $\mathbf{v}$, it can be employed to generate meaningful clusters. Based on the cumulative set of seed vectors and include guards, $\mathbf{V} = \{\tilde{\mathbf{b}}_1, \ldots, \tilde{\mathbf{b}}_q, \mathbf{t}_1, \ldots, \mathbf{t}_t\}$, we gain the strict partitioning

$$C_k = \{\mathbf{x}_i \,|\, k = \operatorname{argmax}_{k \in \{1,\ldots,q+t\}} T(\mathbf{x}_i; \mathbf{V}[k])\} \tag{2}$$

The include guard clusters $C_{q+1}, \ldots, C_{q+t}$ potentially contain target spectra and are hence collected into a rejection class. The endmember matrix $\mathbf{B} = [\mathbf{b}_1, \ldots, \mathbf{b}_q]$ is obtained using the cluster means $\mathbf{b}_k = \frac{1}{|C_k|} \sum_{\mathbf{x}_l \in C_k} \mathbf{x}_l$. As stated before, in Eq. (2) an arbitrary full-pixel target detection algorithm can be employed for the choice of T_D. For computation performance purposes we chose the NCC algorithm for this task. An example of ABGP operation in an artificial hyperspectral image is given in Figure 1. The data set was generated using the LMM as a data generation model using measured background and target spectra as input. The abundances were chosen to create four background regions and a pentaerythritol tetranitrate (PETN) contaminated region in the image center in the form of the Fraunhofer logo with decreasing mixture weight from top to bottom. We show the results of the clustering stage by indicating the location of the chosen spectra. The clustering results are given as indexed color maps where pixel vectors belonging to the same cluster are identically colored. Based on trinitrotoluene (TNT) as target include guard, the ABGP algorithm generated a seed vector for every material region of the image, including the contaminated area. If the PETN library spectrum is employed as include guard, the high PETN contamination area is omitted and the redundant endmember is placed in one of the background regions.

3 Residue detection using active MIR hyperspectral imaging

We demonstrate detection results obtained on measurements acquired with a QCL-based active MIR hyperspectral image sensor (see [9, 11]). The system utilizes two broadly tunable EC-QCLs as illumination sources that offer a cumulative tuning range from 990 cm^{-1} to 1330 cm^{-1}. The EC-QCLs are operated in pulsed mode at 1.7 MHz with a duty cycle of 17%, which leads to an effective emission linewidth of about 1 cm^{-1}. Littrow-type external cavity resonators are employed for controlling the emission wavelength and beam alignment is achieved using a custom-coated dichroitic mirror. The diffusely backscattered light is collected by a high-performance

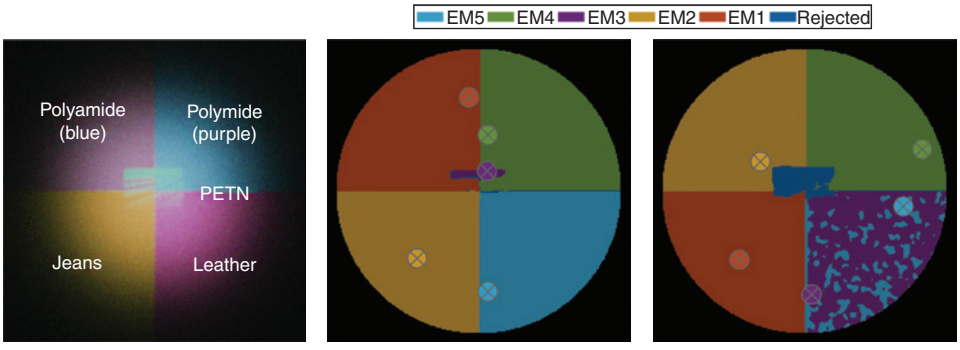

Figure 1: Left: pseudo-color representation of artificial hyperspectral image comprising four different background regions and a PETN contamination. Center: ABGP result for the TNT target hypothesis. The endmember locations are indicated by circled crosses and the spatial regions that form the corresponding cluster are colored accordingly. Right: same for the PETN hypothesis.

mercury-cadmium-telluride (MCT) image sensor that generates 192×192 pixels at a rate of 400 fps. The laser and camera are synchronized by activating the illumination in each second image grabbed by the camera only. The difference of two adjacent frames is used as a signal image to suppress the thermal background of the scene. A multi-look approach is chosen for the reduction of speckle, which stems from the coherent nature of the laser. A series of 10 independent speckle patterns are projected onto the scene and averaged per illumination wavelength. By synchronous step-tuning the emission wavelength, a hyperspectral image is generated with a typical resolution of 1 cm^{-1}. In this configuration full hyperspectral images are acquired in 10 s to 15 s. A set of backscattering spectra measured using the proposed hyperspectral image sensor is shown in Figure 2. All substances show characteristic absorption features in the considered wavelength range. This set serves as spectral library for the suggested detection process in the following.

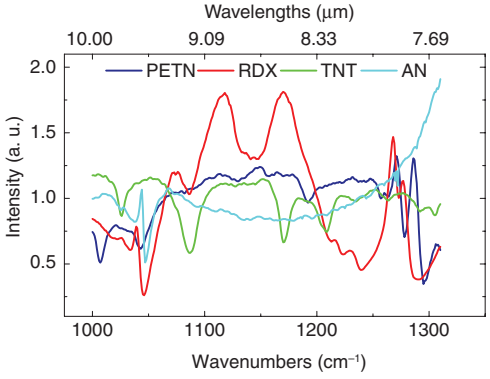

Figure 2: Backscattering spectra of hazardous substances measured using active hyperspectral imaging on a weakly scattering surface (glass).

3.1 Analysis of ABGP operation

In Figure 3 we present the output of the ABGP algorithm on a hyperspectral image of an hexogen (RDX) contaminated polyamide sample. The seed vector locations are indicated as circled colored crosses, and the result of the clustering stage is given as a color map. We show the results obtained under the PETN and RDX hypotheses. Under the PETN hypothesis the ABGP chose the first two endmembers to account for the polyamide substrate. The third endmember fell into an RDX contaminated area that is hence correctly considered background. The clustering results show a random distribution of endmembers 1 and 2 within the background area, indicating a fairly homogeneous substrate material and illumination. Under the RDX hypothesis, the pixel vectors within the target contaminated areas fall into the rejection class and the three background endmember clusters are randomly distributed across the remaining scene.

3.2 Comparison of detection algorithms

In Figure 4 we present a comparison of the detection results obtained by the mentioned methods for the case of PETN residues on a polyamide substrate. The samples were manufactured by deposition of target material on a polyamide substrate using a synthetic rubber stamp. We note that although this approach does not allow us to assess the deposited quantity, it is well suitable to match the morphology of residues to be expected under real world conditions. We follow that all considered model-based sub-pixel detectors (AMSD-ABGP, ACE and OSP) are well applicable to detection in hyperspectral images acquired with the proposed measurement technique and significantly outperform the full pixel detectors. Whereas

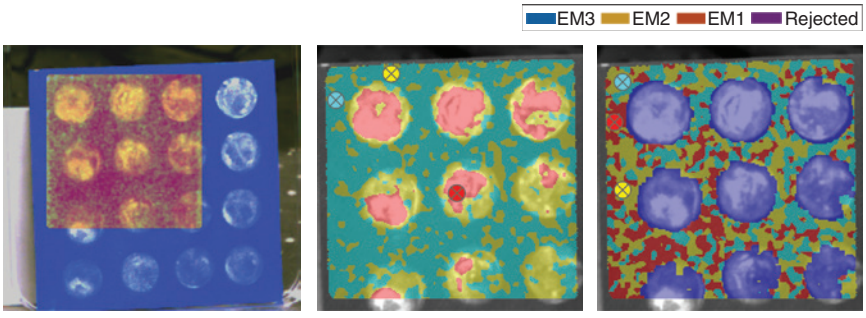

Figure 3: Left: polyamide sample containing RDX contaminated areas transparently overlaid with mean backscattering signal indicating the illuminated region. Center, right: the output of the ABGP algorithm for background endmember extraction under the PETN (center) and RDX (right) target hypothesis.

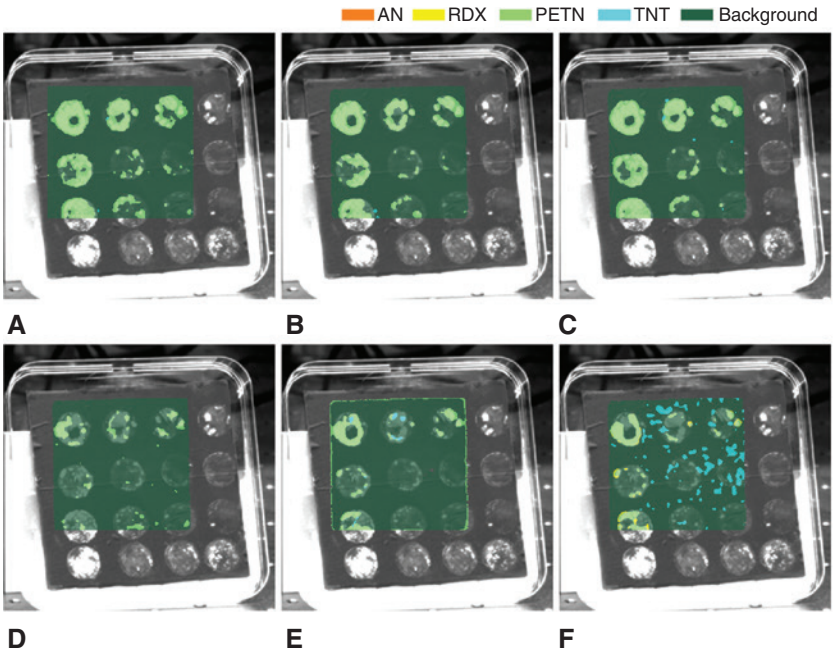

Figure 4: Comparison of the detection results obtained by the considered target detection algorithms on a polyamide sample containing PETN contaminated areas. (A) AMSD-ABGP, (B) ACE, (C) OSP-ABGP, (D) CEM, (E) MF, (F) NCC.

the sub-pixel detectors are capable of detecting lower residue concentrations, the full pixel detectors yield successful detection results only for areas with high target coverage. Among the full pixel detectors, the CEM detector slightly outperforms the MF and NCC detectors. The MF is prone to both false alarms of TNT and false alarms of PETN at the edges of the illuminated area. Considerable false alarm rates for TNT are observed in the detection map generated by the NCC detector.

In Figure 5 we present AMSD-ABGP detection results of PETN, RDX and TNT residues. We observe that all RDX and PETN contaminated areas generated positive detection results with only minor false alarms raised for the competing substances. For the case of TNT contaminants on polyamide the detection outcome is slightly inferior, as one of the contamination areas failed to cause an alarm. Using the background and contaminated spectra obtained by spatial averaging over the corresponding regions as generated in the detection step we obtain a close match of the TNT library spectrum, which supports the assumption that the LMM holds for the suggested measurement principle. We recall that a fundamental assumption of the LMM is that each image spectrum stems from a specific area in the scene, the elongation of which is predominantly defined by the diffraction limited resolution. At the longwave cutoff of the considered configuration this amounts to $d_{\text{airy}} \approx 50$ µm and yields a spatial resolution of 0.68 µm. Hence, any spatial displacement that exceeds this order of magnitude during the measurement potentially induces significant material mixture in single spectra and thus violates the LMM. Consequently, the application of this device is mainly restricted to static scenes.

4 Fast backscattering spectroscopy

In this section we present a modification of the measurement principle that allows real-time spectroscopy and consequently enables remote substance detection in dynamic environments. This is achieved by replacing the mechanically tuned EC-QCL by a rapid wavelength-scanning micro-opto-electro-mechanical system (MOEMS)-tuned EC-QCL device that was developed in collaboration with Fraunhofer IPMS and enables a full wavelength scan at a timescale of ≈1 ms [10, 12]. This renders measured spectra up to a limited timescale invariant to relative motion of the sensor and sample.

4.1 Experimental setup

The MOEMS scanning grating that acts as a wavelength selective element in the Littrow-type external resonator oscillates at its resonance frequency of $f_r = 976$ Hz with an amplitude of $A_0 \approx 4.5°$. A QCL chip tunable in

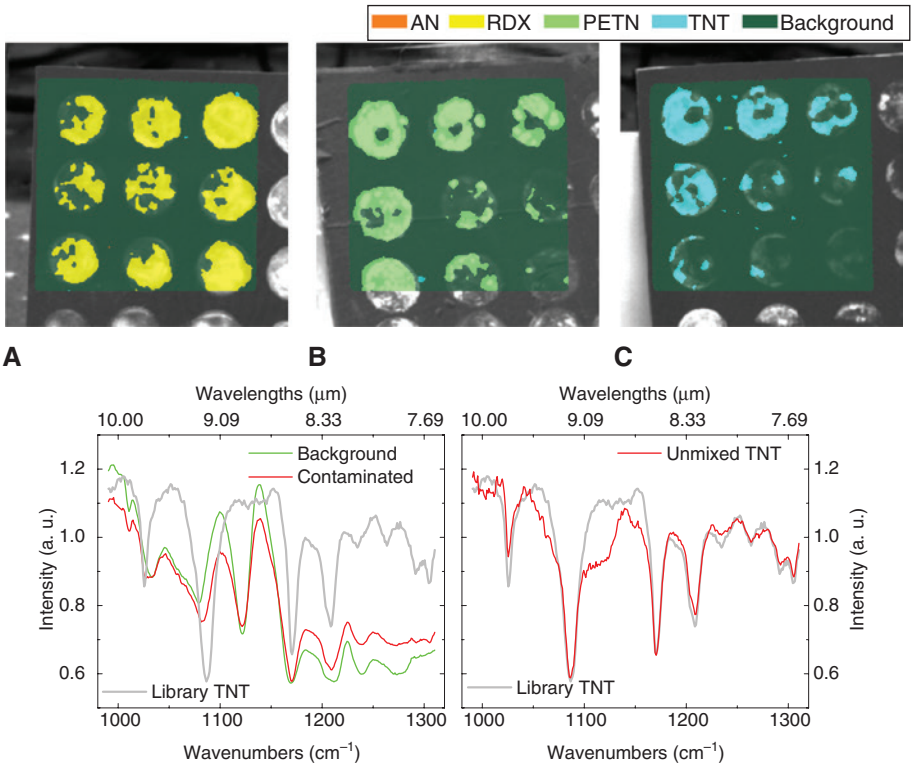

Figure 5: Detection results of RDX (left), PETN (center) and TNT (right) residues on polyamide obtained using the AMSD-ABGP target detection algorithm. Bottom: validation of the linear mixture model for the case of TNT on a polyamide substrate. (A) RDX, (B) PETN, (C) TNT.

the range from 1080 cm^{-1} to 1370 cm^{-1} was used in the MOEMS resonator, and thermoelectric-cooled photovoltaic MCT single-element detectors were employed as signal and reference detectors. The MOEMS grating is tilted at an angle of $\alpha_0 = 33.3°$ relative to the laser chip axis to roughly match the QCL chip's gain spectrum center of ≈1200 cm^{-1}. The laser pulse frequency was set to $400 \cdot f_r$, to gain a fixed phase relation and constant number of evenly time distributed laser pulses per oscillation period. Hence, assuming a perfect harmonic oscillation of the grating, the emission wavelength can be written as discrete time series that can be approximated as

$$\lambda[t] = 2g\sin(\alpha_0 + A_0 \cdot \sin(2\pi f_r t + \phi_0)), \quad (3)$$

where the phase offset ϕ_0 denotes the arbitrary choice of time origin $t = 0$ and $g = 133$ mm denotes the groove density of the diffraction grating etched into the MOEMS mirror. During the 200 ns laser pulse the expected wavelength shift is 0.1 cm^{-1} and hence resides well below the chip's general emission resolution of ≈1 cm^{-1} at a fixed grating position. Due to the sinusoidal time dependence of the emission wavelength the effective spectral measurement resolution is non-constant. An estimate of the obtained resolution for the considered parameters is shown in Figure 6. The angular trajectory of the MOEMS is given as a scatter plot showing the amplitude at the equidistant time stamps defined by the laser pulse train. A spectral resolution of 1.43 cm^{-1} is obtained on average over the full period. Whereas the wavenumber spacing is minimal at the turning points of the oscillatory motion, it increases up to 2.3 cm^{-1} when passing the equilibrium position. This is however sufficient for resolving the broad spectral features observed in spectroscopy of solids.

4.2 Measurement results

We demonstrate the capability of the real-time backscattering spectroscopy device in dynamic scenes employing the samples and algorithms introduced in the previous section. We note that for the application of the model-based algorithms, we require a hyperspectral observation that contains both target and background areas of the scene to be analyzed. This can be achieved by recording a data stream during a scanning motion of either the measurement spot or the sample. While in a hand-held variant of the device this motion would be performed by the operator or a scanning mirror, the data presented

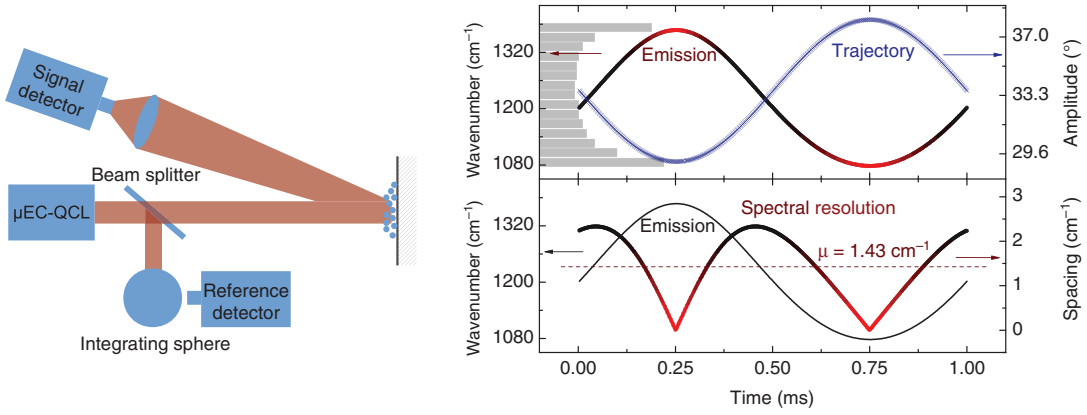

Figure 6: Left: measurement configuration for fast backscattering spectroscopy. Right: estimation of expected spectral resolution. The sampling density is color coded in the wavenumber emission diagram with red indicating higher spectral resolution.

in the following were collected by moving the sample under a fixed measurement spot. The latter is defined by the QCL's collimated output beam that has an approximate 4σ diameter of 3 mm at the measurement distance of 50 cm. Given the approximate average motion speed of 7.5 cm/s, the spatial displacement during a single spectrum acquisition can be estimated to be 76 μm, which resides well below the beam diameter. It can

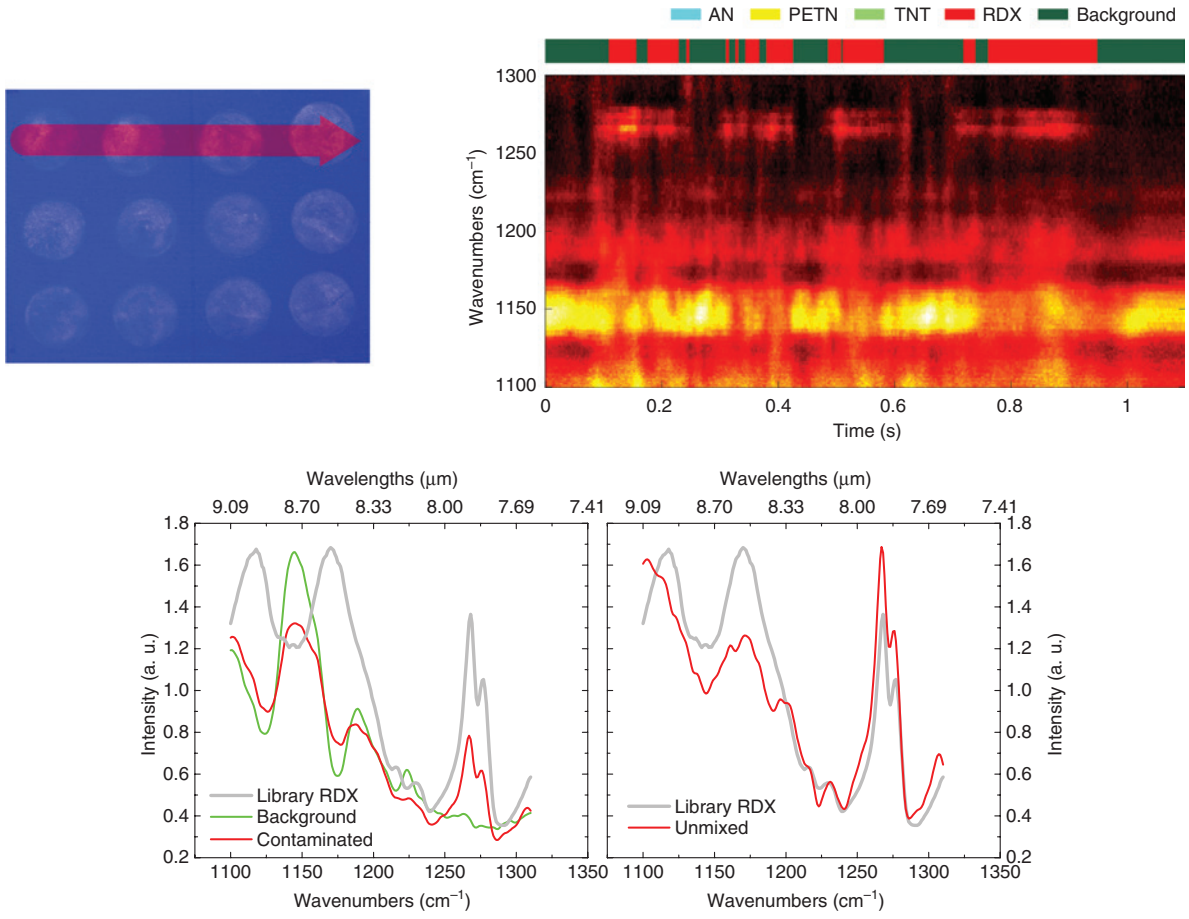

Figure 7: Top: illumination path (left) and detection results (right) of RDX traces on a polyamide surface using real-time backscattering spectroscopy. The detection results are given in the color-coded ribbon at the top of the figure, and were obtained using the AMSD-ABGP target detection algorithm. Bottom: spectral unmixing verifies the application of the LMM as the mixture model.

therefore be assumed that the motion does not induce non-linear mixing effects between adjacent materials. We note that – allowing up to a half beam diameter shift during a full MOEMS oscillation period – under the given measurement parameters a displacement speed of up to 1.54 m/s can be accepted before spatial undersampling occurs and severe non-linear mixing effects are expected at material borders. At the cost of spatial resolution loss the measurement technique can be readily optimized for even higher displacement speeds by increasing the beam diameter. A sample measurement of an RDX contaminated polyamide substrate is shown on the left of Figure 7. The hyperspectral data set containing 1007 samples was recorded in 1.10 s and analyzed using the AMSD algorithm with the proposed ABGP algorithm for background endmember extraction. The measured spectrogram is shown on the right of Figure 7 as an intensity map, and the detection results are given in the color-coded ribbon. The four disjoint contamination areas are observed as positive detection result clusters in the detection output. Based on the segmentation of the observation data induced by the AMSD detection output, we show the mean spectra of contaminated and background subsets in Figure 7. The RDX characteristic features between 1250 cm^{-1} to 1280 cm^{-1} are well observable in the contaminated mean spectrum. We also show that the library spectrum can be obtained from the mean spectra by using linear unmixing, which indicates that the LMM is well applicable for the analysis of hyperspectral image data generated by the fast backscattering spectroscopy measurement principle.

5 Conclusions

Based on Ren and Chang's ATGP algorithm [8], a background extraction method called ABGP was proposed for estimating a set of robust and physically meaningful background spectra in hyperspectral images and employed for operating the AMSD as the target detection algorithm. The resulting AMSD-ABGP detector resembles a fully generic target detection algorithm that requires no knowledge of the background material spectra in the image and was shown to be capable of detecting PETN, TNT and RDX residues in hyperspectral images acquired using active MIR backscattering spectroscopy in static scenes. A real-time capable rapid-wavelength scanning variant based on the same spectroscopy principle was shown to produce measurement data that follow the LMM even in dynamic scenes and the AMSD-ABGP algorithm was successfully employed for contact-less residue detection in the acquired data. This allowed for real-time detection of hazardous substance residues on the surface of moving objects and has the potential to be implemented in a hand-held measurement device.

Acknowledgments: The authors want to thank C. Schilling, Q. Yang, R. Aidam, W. Bronner, R. Driad, S. Adler and U. Weinberg for expert design, fabrication, and testing of the QCL chips used in the presented experiments. J. Jarvis, M. Haertelt, S. Hugger, F. Fuchs, R. Ostendorf, J. Wagner and J. Beyerer conceived and designed the experiments; J. Jarvis, M. Haertelt, S. Hugger and L. Butschek performed the experiments; J. Jarvis, M. Haertelt and S. Hugger wrote the paper.

Funding: Part of the research leading to these results has received funding from the European Communitys Seventh Framework Program (FP7/2007–2013) under Grant Agreements No 317884 MIRIFISENS and the Horizon 2020 program under Grant Agreements 645535 CHEQUERS and 688265 MIRPHAB.

References

[1] C. W. Van Neste, L. R. Senesac and T. Thundat, Appl. Phys. Lett. 92, 234102 (2008).
[2] C. A. Kendziora, R. Furstenberg, M. Papantonakis, V. Nguyen, J. Byers, et al., Appl. Opt. 54, F129–F138 (2015).
[3] H. Östmark, M. Nordberg and T. E. Carlsson, Appl. Opt. 50, 5592–5599 (2011).
[4] J. L. Gottfried, F. C. De Lucia, C. A. Munson and A. W. Miziolek, Anal. Bioanal. Chem. 395, 283–300 (2009).
[5] W. H. Farrand and J. C. Harsanyi, Remote Sens. Environ. 59, 64–67 (1997).
[6] X. Jin, S. Paswaters and H. Cline, Proc. SPIE 7334, 73341W (2009).
[7] D. Manolakis, G. Shaw and N. Keshava, Proc. SPIE 4049, 2–17 (2000).
[8] H. Ren and C. I. Chang, IEEE Trans Aerosp. Electron. Syst. 39, 1232–1249 (2003).
[9] F. Fuchs, S. Hugger, Q. Yang, J. Jarvis, M. Kinzer, et al., in 'The Wonder of Nanotechnology: Quantum Optoelectronic Devices and Applications', Vol. 8631, chapter 25 (SPIE, Bellingham, WA, 2013) pp. 645–672.
[10] R. Ostendorf, L. Butschek, S. Hugger, F. Fuchs, Q. Yang, et al., Photonics 3, 28 (2016).
[11] J. Jarvis, F. Fuchs, S. Hugger, R. Ostendorf, L. Butschek, et al., Proc. SPIE 9824, 98240V (2016).
[12] J. Grahmann, A. Merten, R. Ostendorf, M. Fontenot, D. Bleh, et al., Proc. SPIE 8977, 897708 (2014).

Jan Jarvis
Fraunhofer Institute for Applied Solid State
Physics, (IAF), Tullastrasse 72, 79108 Freiburg, Germany
jan-philip.jarvis@iaf.fraunhofer.de

Jan Jarvis received the Diploma in Computer Science from the Karlsruhe Institute of Technology in 2011. He has since been working at Fraunhofer IAF on stand-off spectroscopy using active QCL-based hyperspectral imaging for detection of hazardous substances. His current research interest lies in data analysis, statistical modeling and signal processing.

Marko Haertelt
Fraunhofer Institute for Applied Solid State Physics
(IAF), Freiburg, Germany

Marko Haertelt received his diploma degree in Physics from the Technische Universitt Berlin in 2008. He worked as a research assistant at the Fritz-Haber-Institute of the Max-Planck-Society in Berlin (Germany) from 2008 to 2012, and received his PhD from the Technische Universitt Berlin in 2012. From 2012 to 2015 he worked as a postdoctoral fellow at the Joint Attosecond Science Laboratory of the University of Ottawa and the National Research Council of Canada. He joined the Fraunhofer IAF in 2016.

Stefan Hugger
Fraunhofer Institute for Applied Solid State Physics
(IAF), Freiburg, Germany

Stefan Hugger received the Diploma in Physics from the University of Freiburg (Germany) in 2003 and the PhD in Physics from the University of Dsseldorf (Germany) in 2008. He joined the Fraunhofer Institute for Applied Solid State Physics in Freiburg, Germany, in 2008. His current research focuses on external cavity QC lasers and their applications in spectroscopy.

Lorenz Butschek
Fraunhofer Institute for Applied Solid State Physics
(IAF), Freiburg, Germany

Lorenz Butschek received his diploma degree in Physics from the University of Innsbruck (Austria) in 2014. He has since been working as a PhD student at Fraunhofer IAF on miniaturized external cavity QCLs. His current research focuses on spectral stability and intensity noise for spectroscopic applications.

Frank Fuchs
Fraunhofer Institute for Applied Solid State Physics
(IAF), Freiburg, Germany

Frank Fuchs received the PhD degree in Physics from Freiburg University, Freiburg, Germany, in 1991. Since then he has carried out applied research at the Fraunhofer Institute for Applied Physics (IAF), Freiburg, Germany. During 2004–2005, he worked as a visiting scientist at the Center for Quantum Devices at Northwestern University, Evanston, IL. His research interests include work on infrared devices based on InAs/GaSb type II heterostructures. Since 2005 he has been concentrating on standoff detection of explosives and detection of hazardous substances in drinking water using broad-band tunable quantum cascade lasers as a key component. Most recently he has moved away from research on civil security and joined the research activities at IAF on solar-blind imaging UV detection based on the AlGaN materials system. He has co-authored more than 100 refereed journal articles and 2 book chapters, contributed in the edition of Landolt-Börnstein, and presented 20+ invited talks on international conferences.

Ralf Ostendorf
Fraunhofer Institute for Applied Solid State Physics
(IAF), Freiburg, Germany

Ralf Ostendorf received his PhD degree in Physics from University of Muenster, Germany, in 2005. His PhD research focused on the analysis of electronic states on surfaces of wide bandgap semiconductor materials. In 2007 he joined the Fraunhofer Institute for Applied Solid State Physics (IAF) in Freiburg, Germany, where he was involved in the development of GaAs-based high-power diode lasers in the near infrared. In 2009 he started working in the development of semiconductor lasers and quantum cascade lasers in the mid-IR range with special focus on QCL-based external cavity laser modules and MIR sensing systems based on this technology. Since the beginning of 2016 he has been the head of the business unit ‘Semiconductor Lasers’ at Fraunhofer IAF.

Joachim Wagner
Fraunhofer Institute for Applied Solid State Physics
(IAF), Freiburg, Germany

Joachim Wagner received the PhD degree in Physics from the University in Stuttgart, Germany, in 1982. From 1982 to 1984 he worked at the ‘Max-Planck-Institut fr Festkrperforschung, Stuttgart, Germany, in the group of Prof. M. Cardona before joining the Fraunhofer-Institute for Applied Solid State Physics, Freiburg, Germany, in 1985. There he is currently Deputy Director and Division Director, responsible for the institute’s business units. He is also Professor at the Institute of Physics of the University of Freiburg and an associated member of the Materials Research Center Freiburg (FMF). His current research interests include III/V-semiconductor-based optoelectronic devices in particular for the infrared spectral range, as well as their integration into modules and sensing systems. He is author or coauthor of 470 scientific publications including several review papers and book chapters.